solar

MDPI

Article

Optimization of Inverted All-Inorganic $CsPbI_3$ and $CsPbI_2Br$ Perovskite Solar Cells by SCAPS-1D Simulation

Carlos Pinzón [1], Nahuel Martínez [1,2], Guillermo Casas [1], Fernando C. Alvira [1], Nicole Denon [3], Gastón Brusasco [4], Hugo Medina Chanduví [5], Arles V. Gil Rebaza [4,5] and Marcelo A. Cappelletti [3,6,*]

1 Laboratorio de Simulación Control Biofotónica y Nanotecnología (SiCoBioNa), Science and Technology Department, Universidad Nacional de Quilmes, Roque Saenz Peña N° 352, Bernal 1876, Argentina
2 CIFICEN (UNCPBA-CICPBA-CONICET), Pinto N° 399, Tandil 7000, Argentina
3 Programa TICAPPS, Universidad Nacional Arturo Jauretche, Av. Calchaquí N° 6200, Florencio Varela 1888, Argentina
4 Departamento de Física, Facultad de Ciencias Exactas, Universidad Nacional de La Plata (UNLP), La Plata 1900, Argentina
5 Instituto de Física La Plata (IFLP), CCT La Plata—CONICET, La Plata 1900, Argentina
6 Grupo de Control Aplicado (GCA), Instituto LEICI (UNLP-CONICET), Facultad de Ingeniería, Universidad Nacional de La Plata, La Plata 1900, Argentina
* Correspondence: marcelo.cappelletti@ing.unlp.edu.ar

Abstract: Perovskite solar cells (PSCs) have substantially increased their power conversion efficiency (PCE) to more than 25% in recent years. However, the instability of these devices is still a strong obstacle for their commercial applications. Recently, all-inorganic PSCs based on $CsPbI_3$ and $CsPbI_2Br$ as the perovskite layer have shown enhanced long-term stability, which makes them potential candidates for commercialization. Currently, all-inorganic PSCs with inverted p-i-n configuration have not yet reached the high efficiency achieved in the normal n-i-p structure. However, the inverted p-i-n architecture has recently drawn attention of researchers because it is more suitable to prepare tandem solar cells. In this work, a theoretical study of inverted p-i-n all-inorganic PSCs based on $CsPbI_3$ and $CsPbI_2Br$ as the perovskite layer was carried out using SCAPS-1D software (ver. 3.3.09). The performance of different architectures of PSC was examined and compared by means of numerical simulations using various inorganic materials as the hole transport layer (HTL) and the electron transport layer (ETL). The results reveal that CuI and ZnO are the most suitable as HTL and ETL, respectively. In addition, the performance of the devices was significantly improved by optimizing the hole mobility in CuI as well as the thickness, doping density, and defect density in the absorber layer. Maximum efficiencies of 26.5% and 20.6% were obtained under optimized conditions for the inverted all-inorganic $CsPbI_3$- and $CsPbI_2Br$-based PSCs, respectively. These results indicate that further improvements in the performance of such devices are still possible.

Keywords: all-inorganic perovskite solar cells; $CsPbI_3$; $CsPbI_2Br$; inverted p-i-n architecture; numerical simulations

Citation: Pinzón, C.; Martínez, N.; Casas, G.; Alvira, F.C.; Denon, N.; Brusasco, G.; Medina Chanduví, H.; Gil Rebaza, A.V.; Cappelletti, M.A. Optimization of Inverted All-Inorganic $CsPbI_3$ and $CsPbI_2Br$ Perovskite Solar Cells by SCAPS-1D Simulation. *Solar* **2022**, *2*, 559–571. https://doi.org/10.3390/solar2040033

Academic Editors: Dewei Zhao and Jürgen Heinz Werner

Received: 16 September 2022
Accepted: 28 November 2022
Published: 9 December 2022

1. Introduction

The increase in energy consumption in recent years has promoted the use of new technologies based on renewable energy sources to generate electricity, with solar energy being one of the most promising alternatives. In this way, the study of solar cells, devices capable of converting light from the sun directly into electricity, is extremely important today. The study of microscopic properties of materials, in addition to advances in the manufacturing processes of the photovoltaic devices, has provided a path to develop new technologies in solar cells with higher performance and shorter processing time.

One of the developments that have gained special relevance in the last decade are perovskite solar cells (PSCs), which have emerged as a technology with the potential to

revolutionize the photovoltaic industry. This is mainly due to their excellent optical and electronic properties such as tunable band gap, large absorption coefficient, high charge carrier mobility, long diffusion lengths, their simpler manufacturing process, and lower cost compared with conventional crystalline silicon solar cell [1–3].

The power conversion efficiencies (PCE) of PSCs have substantially increased from 3.8% in 2009 [4] to more than 25% today [5]. The highest efficiencies so far were obtained for the so-called organic–inorganic hybrid PSCs. These consist of a perovskite layer as a light-absorbing region sandwiched between a p-type hole transport layer (HTL) and an n-type electron transport layer (ETL). These devices have achieved efficiencies comparable to technologies already established in the market, such as thin film solar cells based on cadmium telluride (CdTe), copper indium gallium selenide (CIGS), or even, as silicon solar cells. These high-efficiency hybrid PSCs are based on methylammonium ($CH_3NH_3^+$ or MA) lead iodide ($MAPbI_3$) and formamidinium ($NH_2CH{=}NH_2^+$ or FA) lead iodide ($FAPbI_3$) as light-harvesting materials. However, the long-term stability of organic–inorganic hybrid PSCs is still a serious problem because of their potential degradation under chemical and thermal pressure [6], which is a strong obstacle for their further development and commercial application [7,8]. In particular, $MAPbI_3$ has proven to be unstable due to the high volatility of hydrophilic organic cations at high temperature (such as $CH_3NH_3^+$). In comparison with $MAPbI_3$, the $FAPbI_3$ perovskite has shown superior thermal stability and even better photoelectric property [9], but phase stability has been a major cause of concern. $FAPbI_3$ suffers a structural phase transition from black α-phase to non-perovskite yellow δ-phase at room temperature [10,11].

The replacement of volatile organic cations by inorganic components such as cesium (Cs^+) has recently allowed the development of all-inorganic PSCs aiming to improve both the stability and efficiency of the devices [12–17]. All-inorganic $CsPbI_xBr_{3-x}$ perovskite (with x between 0 and 3) have a band gap ranging from 1.73 eV ($CsPbI_3$) to 2.31 eV ($CsPbBr_3$) [18]. $CsPbI_3$ has the most suitable band gap to fabricate high-efficiency PSCs, being therefore an ideal material to prepare tandem devices combined with either silicon or low band gap perovskite solar cells [19,20]. Although $CsPbBr_3$ exhibits a great phase stability, the large band gap limits its efficiency [21]. For its part, $CsPbI_2Br$ perovskite possesses reasonable band gap (close to 1.9 eV) and phase stability, which makes it a great candidate for achieving a highly efficient and stable all-inorganic PSC, especially for the semitransparent and tandem solar cells [22,23].

Most of the high-performance all-inorganic PSCs reported so far are based on the normal n-i-p architecture due to their superiority in performance. $CsPbI_3$ based PSCs in particular, have significantly enhanced the efficiency from 2.9% [24] to over 20% in 2022 [25,26]. On the other hand, a record power conversion efficiency of 17.51% was recently reported for the normal structure (n-i-p) $CsPbI_2Br$ cell [27].

Nowadays, there is increasing interest in the study of the all-inorganic PSCs with inverted p-i-n structure [28–32]. They offer some advantages compared with the conventional n-i-p architecture, such as lower hysteresis in current–voltage characteristics, and improved operability in the tandem solar cell fabrication process [28,29]. Inverted $CsPbI_3$ and $CsPbI_2Br$ cells have recently reached efficiencies of up to 19.27% [33] and 14.62% [32], respectively. These values are still far from 25% for hybrid PSCs; therefore, further studies are needed to identify the factors that limit the performance of p–i–n PSCs. The performance of tandem solar cells can be improved by optimizing the design of the inverted all-inorganic PSCs separately. In this paper, a comparative theoretical analysis of inverted all-inorganic $CsPbI_3$- and $CsPbI_2Br$-based PSCs was conducted using modeling and simulation techniques. These are fundamental tools to predict and analyze the behavior of the photovoltaic cells. Four materials (NiO, Cu_2O, CuSCN, and CuI) were proposed as the inorganic hole-transporting layer (i-HTL); and three materials (ZnO, TiO_2, and SnO_2) were used as the inorganic electron-transporting layer (i-ETL). These inorganic materials under consideration in this study are promising candidates for use in all-inorganic PSCs with inverted structure. The performance of the devices was evaluated for different thicknesses,

acceptor densities, and defect densities in the perovskite layer to optimize the design of the structure and to enhance the efficiency of these inverted all-inorganic PSCs.

2. Simulation Details

2.1. Electronic Structure Calculations

The electronic band structure of the cubic perovskite $CsPbI_3$ with space group Pm-3m and $CsPbI_2Br$ with space group P4/mmm was studied from the first principles theory. These calculations are based on the Density Functional Theory (DFT) [34], and the self-consistent Kohn–Sham equation was solved using the Full-Potential Linearized Plane-Wave method (FP-LAPW) implemented in the Wien2k code [35,36]. The exchange-correlation (XC) functional was described using the Perdew–Burke–Ernzerhof (PBE) parametrization of the Generalized Gradient Approximation (GGA) [37]. In order to improve the electronic band structure of the compounds, the hybrid XC functional proposed by Heyd–Scuseria–Ernzerhof (HSE06) [38] was used. The muffin-tin radii employed was 2.0 bohr for the Cs, Pb, Br, and I atoms, whereas the parameter related with basic-set size was set to $R_{MT} \times K_{max} = 9$ (RMT is the smallest muffin-tin radii and K_{max} is related with the plane-wave cutoff). Regarding the reciprocal space, this was sampled using a dense mesh grid of $12 \times 12 \times 12$ k points in the irreducible Brillouin zone.

The theoretical lattice parameters obtained were 6.398 Å and 6.0023 Å for the $CsPbI_3$ and $CsPbI_2Br$, respectively, which are in agreement with experimental values reported [39–41]. In order to obtain an accurate description of the electronic structures of the $CsPbI_3$ and $CsPbI_2Br$ perovskites, we calculated the total and projected density of state (DOS) and the electronic band gap using the HSE06 hybrid functional, as seen in Figures 1 and 2, respectively. Direct band gaps of 1.78 eV and 1.88 eV were found for the $CsPbI_3$ and $CsPbI_2Br$, respectively, in excellent agreement with the experimental values reported: 1.76 eV [42], 1.77 eV [43], and 1.79 eV [44] for the $CsPbI_3$, and 1.82 eV [13], 1.86 eV [45], and 1.92 eV [46] for the $CsPbI_2Br$. The band gap of the $CsPbI_3$ perovskite is formed between the VBM, p-I orbital, and the CBM, p-Pb orbital. In the case of $CsPbI_2Br$, the band gap is formed between the VBM, p-I, and p-Br orbitals, and the CBM, p-Pb orbital. For both compounds, the orbitals of the Cs atom are located far of the Fermi energy, as is shown in Figures 1 and 2.

2.2. Device Simulations

Device simulations were performed with SCAPS-1D software [47], which is widely used and recognized by the scientific community related to PSCs [3,48–53]. This software numerically solves the system of the Poisson and the continuity equations for electrons and holes. The output parameters such as short-circuit current density (J_{SC}), open circuit voltage (V_{OC}), power conversion efficiency (PCE), maximum power point (P_{MAX}), fill factor (FF), and external quantum efficiency (EQE) can be calculated using the SCAPS-1D software, in order to obtain the response of the device under different design and operating conditions.

Figure 3 shows the configuration of the all-inorganic PSC used in this work, which consists of an inverted structure ITO/i-HTL/$CsPbI_xBr_{3-x}$/i-ETL/Ag, for x equal to 2 and 3, where light enters through the i-HTL. The standard AM1.5G spectrum has been used.

Tables 1–3 summarize the main parameters used in the simulations for the perovskite layers, and for the materials chosen as i-HTL and i-ETL, respectively. Here N_A and N_D are the acceptor and donor density, respectively; ε_r is the relative permittivity; χ is the electron affinity; E_G is the band gap energy; μ_n and μ_p are the electron and hole mobilities, respectively; N_T is the defect density; and N_C and N_V are the effective conduction and valence band density of states, respectively. The band gap energy and N_C and N_V values of Table 1 were obtained by means of DFT-based calculations. The rest of the values in Tables 1–3 are based on experimental and theoretical studies recently reported in the literature [51,54–56]. The absorption coefficient (α) was calculated from the Beer–Lambert law $\alpha = 2.303A/t$ [57], where A and t are the absorbance and thickness of film (350 nm), respectively. These were obtained from Wang 2020 [14] for the $CsPbI_3$ layer and from

Sutton 2016 [13] for the $CsPbI_2Br$ layer. The work functions of the front and back contacts are 4.7 eV (ITO) and 4.26 eV (Ag), respectively [58].

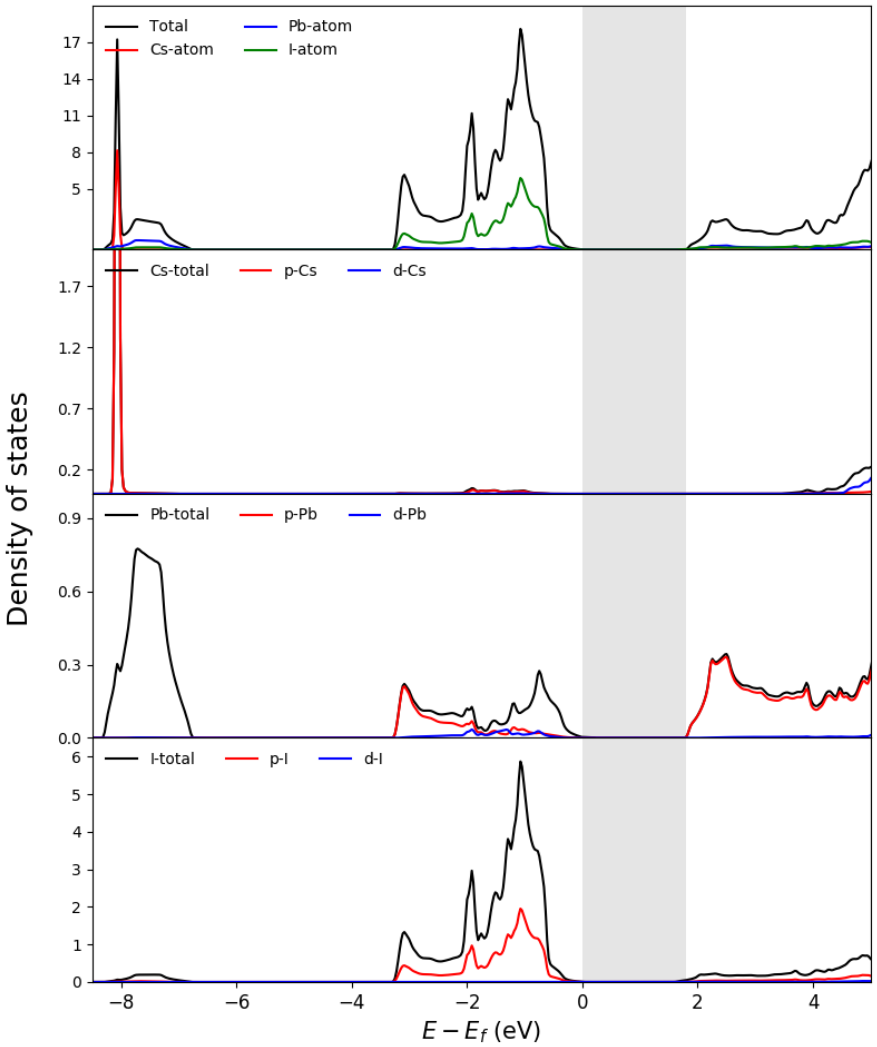

Figure 1. Total and projected density of states of the $CsPbI_3$ compound, showing the electronic band gap of 1.78 eV calculated using HSE06 (grey vertical bar).

The energy level diagram of the i-ETL and i-HTL materials used in the simulation is shown in Figure 4. These levels play an important role in the performance of the device because they have a significant control on photocarrier transport. In order to facilitate proper electron transport, the conduction band minimum of the perovskite layer should be higher than that of the ETL. Similarly, the valence band maximum of the perovskite layer should be lower than that of the HTL for proper hole transport [59].

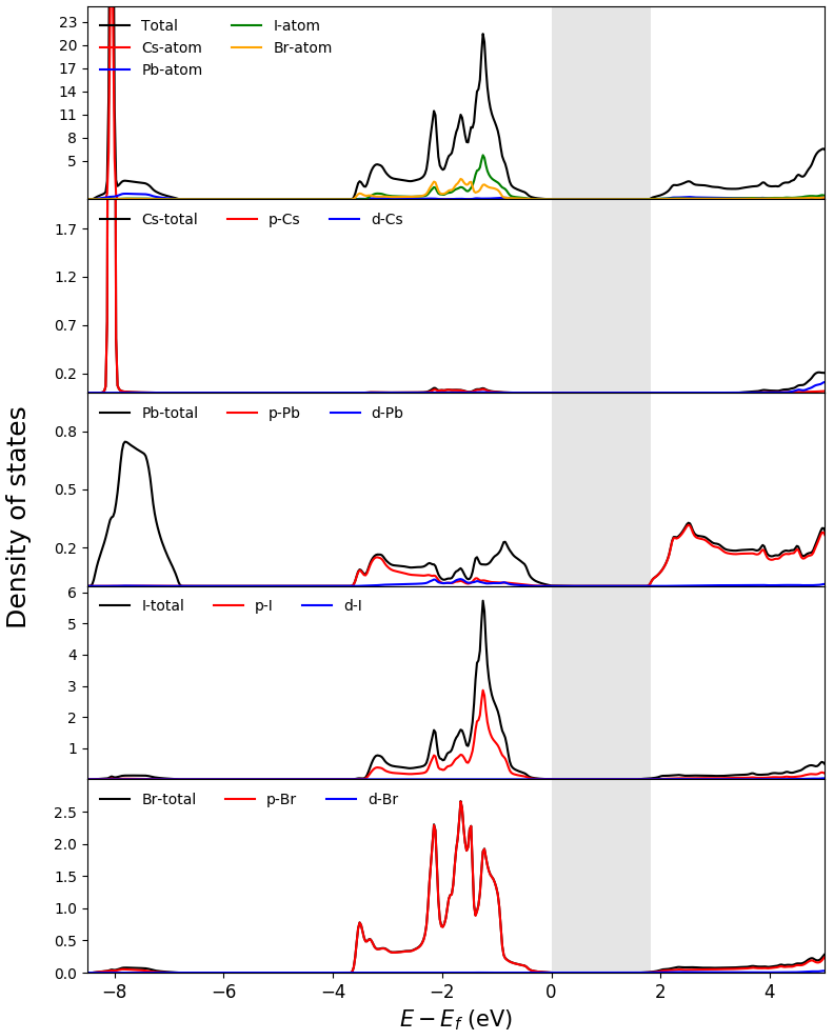

Figure 2. Total and projected density of states of the $CsPbI_2Br$ compound, showing the electronic band gap of 1.88 eV calculated using HSE06 (grey vertical bar).

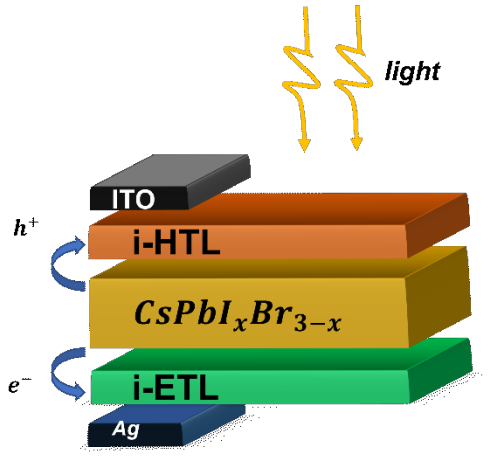

Figure 3. Device architecture of inverted all-inorganic PSC used in this work.

Table 1. Physical parameters of the perovskite material used in the simulation.

Parameters	$CsPbI_3$	$CsPbI_2Br$
Thickness (nm)	350	350
N_A (cm^{-3})	1×10^{15}	1×10^{15}
N_D (cm^{-3})	-	-
ε_r	6	8.6
χ (eV)	3.49	3.73
E_G (eV)	1.78	1.88
μ_n ($cm^2V^{-1}s^{-1}$)	16	25
μ_p ($cm^2V^{-1}s^{-1}$)	16	25
N_T (cm^{-3})	2.07×10^{14}	3.6×10^{16}
N_C (cm^{-3})	1.61×10^{19}	1.90×10^{19}
N_V (cm^{-3})	2.21×10^{18}	2.37×10^{18}

Table 2. Physical parameters of the i-HTL materials used in the simulation.

Parameters	NiO	Cu_2O	CuSCN	CuI
Thickness (nm)	25	25	25	25
N_A (cm^{-3})	3×10^{18}	3×10^{18}	3×10^{18}	3×10^{18}
N_D (cm^{-3})	-	-	-	-
ε_r	11.7	7.11	10	6.5
χ (eV)	1.46	3.2	1.9	2.1
E_G (eV)	3.8	2.17	3.4	3.1
μ_n ($cm^2V^{-1}s^{-1}$)	2.8	200	2×10^{-4}	100
μ_p ($cm^2V^{-1}s^{-1}$)	2.8	80	2×10^{-1}	44
N_T (cm^{-3})	1×10^{17}	1×10^{17}	1×10^{17}	1×10^{17}
N_C (cm^{-3})	2.5×10^{20}	2.5×10^{20}	1.7×10^{19}	2.8×10^{19}
N_V (cm^{-3})	2.5×10^{20}	2.5×10^{20}	2.5×10^{21}	1×10^{19}

Table 3. Physical parameters of the i-ETL materials used in the simulation.

Parameters	ZnO	TiO_2	SnO_2
Thickness (nm)	25	25	25
N_A (cm^{-3})	-	-	-
N_D (cm^{-3})	3×10^{18}	3×10^{18}	3×10^{18}
ε_r	9	9	9
χ (eV)	4	4	4
E_G (eV)	3.16	3.2	3.5
μ_n ($cm^2V^{-1}s^{-1}$)	100	20	20
μ_p ($cm^2V^{-1}s^{-1}$)	25	10	10
N_T (cm^{-3})	1×10^{17}	1×10^{17}	1×10^{17}
N_C (cm^{-3})	4.5×10^{18}	1×10^{21}	4.36×10^{18}
N_V (cm^{-3})	1×10^{18}	2×10^{20}	2.52×10^{19}

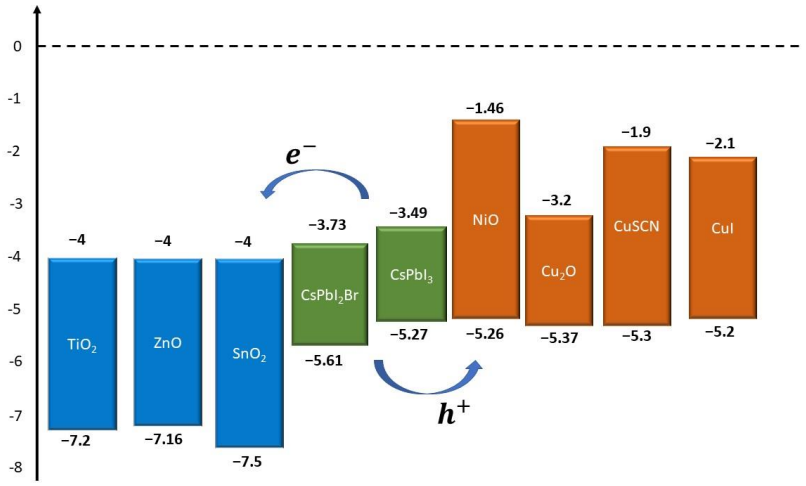

Figure 4. Energy-level diagram of the studied inverted all-inorganic PSCs with different i-ETL and i-HTL.

3. Results and Discussion

Using the values of Tables 1–3, an analysis of the twelve different possible combinations (i-ETL/i-HTL) of the inverted all-inorganic PSCs was carried out by means of SCAPS-1D software for each perovskite layer under study. The results of the output parameters (PCE, V_{OC}, J_{SC}, and FF) are summarized in Table 4. The first row in Table 4 corresponds to the materials used in [14]. The value of PCE of 14.03% obtained from simulations for the ZnO/NiO combination can be considered as a good approximation of the experimental result of 13.90% presented in Table 4 for the control device with the non-passivated perovskite film. It can also be observed in Table 4 that for the $CsPbI_3$- and $CsPbI_2Br$-based PSCs, the V_{OC} values remain almost unchanged for all considered cases. On the other hand, PCE is the parameter with the greatest variations between their minimum and maximum values, approximately 24% and 14%, for the $CsPbI_3$- and $CsPbI_2Br$-based PSCs, respectively.

Table 4. Output parameters of the PSC for the twelve different combinations with 350 nm thick $CsPbI_2Br$ and $CsPbI_3$ considered in this work.

i-ETL/i-HTL	PCE (%)		V_{OC} (V)		J_{SC} (mA/cm^2)		FF (%)	
	$CsPbI_2Br$	$CsPbI_3$	$CsPbI_2Br$	$CsPbI_3$	$CsPbI_2Br$	$CsPbI_3$	$CsPbI_2Br$	$CsPbI_3$
ZnO/NiO	12.32	14.03	0.91	1.29	16.13	13.44	84.42	81.15
SnO_2/NiO	12.31	14.02	0.91	1.29	16.12	13.43	84.41	81.20
TiO_2/NiO	12.19	12.28	0.91	1.29	16.13	13.43	82.97	71.16
ZnO/Cu_2O	11.03	12.99	0.90	1.28	15.33	12.89	79.90	78.86
SnO_2/Cu_2O	11.02	12.97	0.90	1.28	15.32	12.87	79.89	78.89
TiO_2/Cu_2O	10.81	11.42	0.90	1.28	15.33	12.87	78.72	69.32
ZnO/CuSCN	11.89	13.65	0.91	1.29	16.10	13.45	81.58	78.54
SnO_2/CuSCN	11.88	13.56	0.91	1.29	16.09	13.43	81.57	78.42
TiO_2/CuSCN	11.81	11.96	0.90	1.28	16.11	13.43	81.66	69.34
ZnO/CuI	12.35	14.13	0.91	1.29	16.06	13.46	84.90	81.51
SnO_2/CuI	12.34	14.11	0.91	1.29	16.05	13.45	84.89	81.55
TiO_2/CuI	12.23	12.42	0.90	1.29	16.07	13.45	84.56	71.73

For ETL materials, the highest PCE values were obtained for ZnO, while the lowest PCE values were obtained for TiO_2. TiO_2 and ZnO have very similar properties (band structure, electronic affinity, relative permittivity, band gap energy, among others). However, TiO_2 has higher N_C and N_V, and therefore higher intrinsic carrier concentration than ZnO. The larger the intrinsic carrier concentration, the higher the recombination rate and the smaller the carrier collection when the electric field is high (at voltages close to V_{OC}). As a consequence of the aforementioned effects, lower FF and PCE were obtained for TiO_2 compared with ZnO. Therefore, TiO_2 is not the optimal material as ETL for $CsPbI_3$ and $CsPbI_2Br$ perovskite solar cells as considered in this work.

On the other hand, the choice of HTL also influences the performance of the device. The band alignment of the HTL with the perovskite layer and the intrinsic carrier concentration of the HTL material are key factors as well as the band gap and the hole mobility. The energy level diagram shown in Figure 4 indicate that there are good band alignments between the valance band of perovskite and the four HTL materials considered in this work. However, Table 4 shows that for a given ETL, the lowest PCE values were obtained for Cu_2O, while the highest PCE values were obtained for CuI. Although Cu_2O and CuI have similar band alignment and hole mobility, Cu_2O has higher N_C and N_V, and therefore a higher intrinsic carrier concentration and recombination rate than CuI. Cu_2O also has the lowest band gap. Since light enters through the HTL in a direct (p–i–n) structure, some ultraviolet light does not reach the perovskite layer in Cu_2O, resulting in the lowest J_{CC} and PCE.

The highest PCE values of 14.13% (for $CsPbI_3$) and 12.35% (for $CsPbI_2Br$) were obtained for the ZnO/CuI combination. These materials have a suitable band alignment with the

active layer. For this reason, ZnO and CuI can be considered as good options for i-ETL and i-HTL, respectively.

In the rest of this work, PSCs with the inverted structure of ITO/CuI/$CsPbI_3$ ($CsPbI_2Br$) /ZnO/Ag are studied in detail, using different hole mobilities in CuI and different thicknesses, acceptor densities, and defect densities for the perovskite layers.

Figure 5 shows the PCE as a function of hole mobility of CuI HTL for $CsPbI_3$ and $CsPbI_2Br$ PSC. In both cases, PCE is gradually reduced as the hole mobility decreases below a critical value (around 40 $cm^2V^{-1}s^{-1}$), which is directly related to a shorter carrier diffusion length. In a previous work, we have shown a similar result for the $MAPbI_3$ PSCs [52]. When the carrier diffusion length is less than the thickness of the HTL material, most carriers recombine before reaching the contacts. PCE values of 10.5% (for $CsPbI_3$) and 7.8% (for $CsPbI_2Br$) were obtained for the lowest value of hole mobility considered (4×10^{-5} $cm^2V^{-1}s^{-1}$). On the other hand, as hole mobility increases, the carrier diffusion length becomes much greater than the HTL thickness, thereby facilitating carrier transport without significant recombination. Figure 5 shows that the PCE saturates for hole mobility values greater than 40 $cm^2V^{-1}s^{-1}$. Therefore, the hole mobility value of 44 $cm^2V^{-1}s^{-1}$ used in the simulations is appropriate to obtain a better performance of the devices.

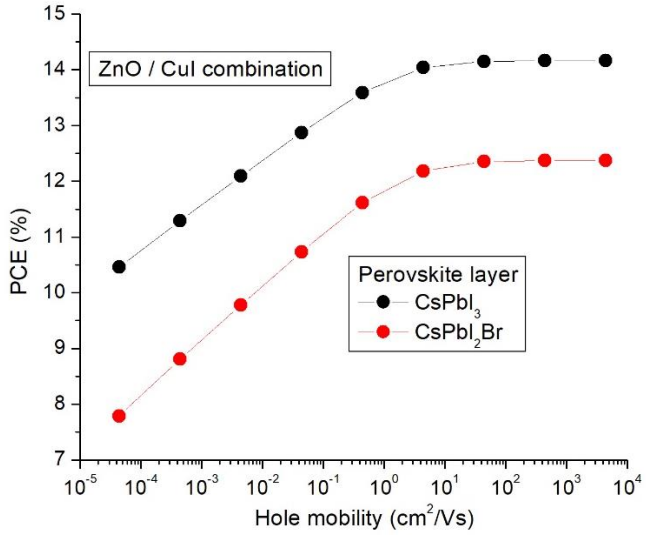

Figure 5. Power conversion efficiency versus hole mobility of CuI HTL for $CsPbI_3$ and $CsPbI_2Br$ perovskite solar cells.

From here, the study was focused on the perovskite layer, in which light is absorbed to produce photo-generated carriers, thus playing a decisive role in the device performance.

Figure 6 shows the J-V characteristics (a) and EQE spectrum (b) for $CsPbI_3$ and $CsPbI_2Br$ devices for two different thicknesses of the absorber film: 350 and 750 nm. We can see that a slight reduction in V_{OC} but a significant increase in J_{SC} were obtained when the absorber thickness increased from 350 to 750 nm. This behavior is consistent with the EQE results. Since it is possible to improve the device efficiency by increasing the absorber thickness, Figure 7 shows the variation in the electrical parameters (PCE, V_{OC}, J_{SC}, and FF) when the $CsPbI_3$ and $CsPbI_2Br$ thickness is increased from 250 nm. The values displayed in this figure are normalized to those corresponding to the thickness of 350 nm, previously shown in Table 4 for ZnO as i-ETL and CuI as i-HTL.

We can see in Figure 7a that when the $CsPbI_3$ thickness increases from 250 to 1750 nm, the V_{OC} and FF decrease by 4% and 35%, respectively. The drop in V_{OC} can be explained by the dependence of this parameter on the photogenerated current and the dark saturation current. An increase in the dark saturation current promotes carrier recombination, which leads to a drop in V_{OC} with increasing thickness. Furthermore, the strong decrease in FF with increasing thickness of the active layer can be explained by the increase in series

resistance. In contrast, the J_{SC} is strongly increased above 80% with increasing $CsPbI_3$ thickness. This remarkable increase is due to the enhanced light absorption and, consequently, a higher concentration of free carriers that can be generated by photons and collected by the electrode. In the case of the PCE parameter, a significant increase by 30% is seen when the thickness is increased from 250 to 750 nm and then it starts to decrease for thicker films.

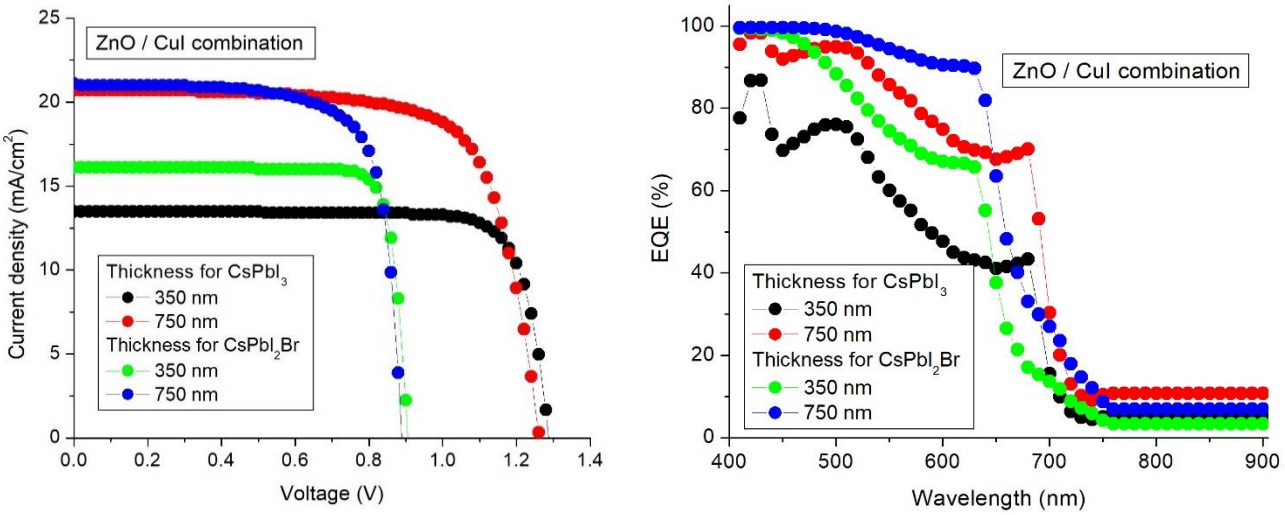

(**a**) (**b**)

Figure 6. J-V characteristics (**a**) and EQE spectrum (**b**) for $CsPbI_3$ and $CsPbI_2Br$ perovskite solar cells.

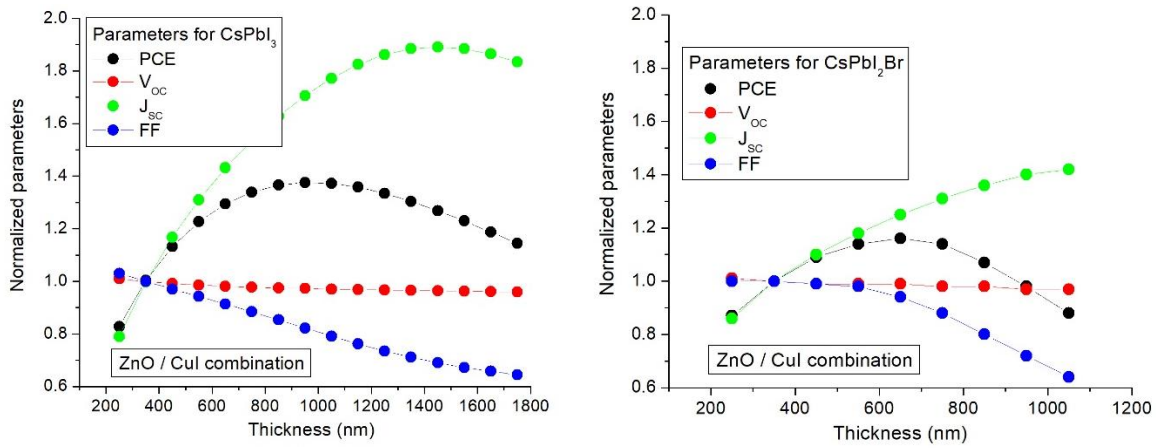

(**a**) (**b**)

Figure 7. Normalized electrical parameters as a function of the (**a**) $CsPbI_3$ and (**b**) $CsPbI_2Br$ absorber thickness.

Similarly, we can see in Figure 7b that when the $CsPbI_2Br$ thickness increases from 250 to 1050 nm, the V_{OC} and FF parameters decrease by 4% and 36%, respectively, whereas J_{SC} increases by 40%, as the increase in the $CsPbI_2Br$ thickness. Furthermore, the PCE value is improved by 15% for a $CsPbI_2Br$ thickness of 650 nm relative to the thickness of 350 nm. Extending the thickness beyond 650 nm increases the recombination current and series resistance and thus reduces the PCE. In the $CsPbI_2Br$ PSC, the maximum value of PCE is reached for a lower thickness compared with the $CsPbI_3$ cell. This is due to the fact that the defect density in the $CsPbI_2Br$ layer is two orders of magnitude higher than in $CsPbI_3$ (see Table 1), which reduces the carrier diffusion length. Therefore, values of 750 nm and 650 nm were considered as the optimized values of the $CsPbI_3$ and $CsPbI_2Br$ absorber thickness, respectively.

On the other hand, Figure 8 shows the variation of the PCE as a function of the acceptor density in the $CsPbI_3$ and $CsPbI_2Br$ perovskite layer, respectively. We can see in both cases that when the acceptor density increases from 10^{13} to 10^{15} cm^{-3}, the PCE remains constant, while this parameter decreases for higher values of 10^{15} cm^{-3}. Therefore, an optimal value of 10^{15} cm^{-3} was chosen for N_A.

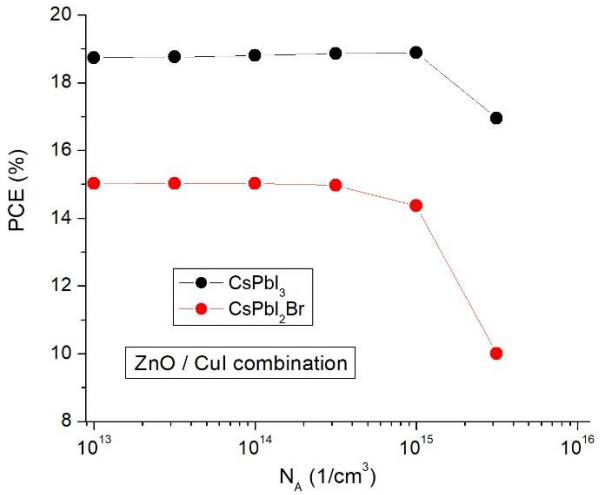

Figure 8. PCE as a function of the acceptor density.

Finally, the simulation results show that when optimized parameters are used with the $CsPbI_3$- and $CsPbI_2B$-based PSCs with the fixed values of N_T presented in Table 1, the PCE values increase from 14.13% to 18.9% and from 12.35% to 14.37%, respectively, such as is shown in Figure 9. Additionally, this figure shows that the defect density N_T of the perovskite layer has a significant impact on device performance. This is because more defects in the active layer shorten the minority-carrier diffusion length, and hence the photogenerated carriers recombine before reaching their respective electrode and thus do not contribute to improving device performance. Figure 9 shows the performance improvement that could be achieved by reducing the defect density. Optimum efficiencies of 26.5% and 20.6% could be obtained at defect density of the order of 10^{12} cm^{-3} for the inverted device with a structure of ITO/CuI/$CsPbI_3$/ZnO/Ag and ITO/CuI/$CsPbI_2Br$/ZnO/Ag, respectively.

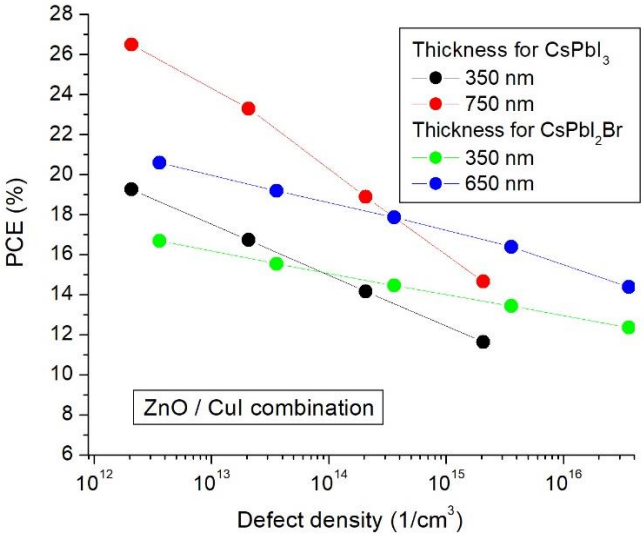

Figure 9. PCE as a function of the defect density.

4. Conclusions

Inverted p-i-n all-inorganic PSCs based on $CsPbI_3$ and $CsPbI_2Br$ perovskite were studied through SCAPS-1D simulations. For each perovskite layer considered, the performance of twelve architectures of PSC was examined and compared, using several potential inorganic materials for HTL and ETL. The simulation results show that CuI as HTL and ZnO as ETL have better performance than the other combinations considered in this study, with efficiencies of 14.13% and 12.35% for $CsPbI_3$ and $CsPbI_2Br$, respectively, which is due to proper band alignment with the absorber. In order to improve the performance of ITO/CuI/$CsPbI_3$/ZnO/Ag and ITO/CuI/$CsPbI_2Br$/ZnO/Ag, the optimal values of hole mobility in CuI and the thickness, doping density, and defect density in the absorber layer were obtained. Values of 44 $cm^2V^{-1}s^{-1}$ and 10^{15} cm^{-3} were chosen for hole mobility in CuI and doping density, respectively. Additionally, values of 750 nm and 650 nm were considered as the optimized values of the $CsPbI_3$ and $CsPbI_2Br$ absorber thickness, respectively. From these optimal values, improved efficiencies of 18.9% and 14.37% were achieved for the $CsPbI_3$- and $CsPbI_2Br$-based PSCs respectively. Finally, maximum efficiencies of 26.5% and 20.6% could be obtained by reducing the defect density up to the order of 10^{12} cm^{-3} for the $CsPbI_3$ and $CsPbI_2B$ devices, respectively. The results obtained in this work are helpful for improving the performance of inverted all-inorganic PSCs based on $CsPbI_3$ and $CsPbI_2B$ as the perovskite layer, which is also essential to optimize the performance of tandem solar cells.

Author Contributions: Conceptualization, A.V.G.R. and M.A.C.; methodology, G.C. and F.C.A.; software, C.P. and N.M.; validation, G.B., H.M.C. and N.D.; formal analysis, F.C.A., M.A.C. and G.C.; investigation, C.P. and N.M.; data curation, C.P. and N.M.; writing—original draft preparation, M.A.C., N.M. and C.P.; writing—review and editing, F.C.A., A.V.G.R. and G.C.; supervision, M.A.C. All authors have read and agreed to the published version of the manuscript.

Funding: This work was partially supported by the National Council Research (CONICET), Argentina under contract PIP-1460; the Province of Buenos Aires, Argentina, through the Convocatoria a Proyectos de Investigación y Transferencia del Colaboratorio Universitario de Ciencias, Artes, Tecnología, Innovación y Saberes del Sur (CONUSUR), Proyecto: "Design and development of low-cost photovoltaic devices based on materials with perovskite structure"; the Universidad Nacional de Quilmes, Argentina under contract #1303/19; the Universidad Nacional de La Plata, Argentina under contract PID-I258; the Universidad Nacional Arturo Jauretche, Argentina; the Universidad Nacional del Centro de la Provincia de Buenos Aires, Argentina; and Proyecto IPAC 2019—Supercomputadora TUPAC, Centro de Simulación Computacional para Aplicaciones Tecnológicas CSC-CONICET, SNCAD-MINCyT, Argentina.

Institutional Review Board Statement: Not applicable.

Informed Consent Statement: Not applicable.

Data Availability Statement: Not applicable.

Conflicts of Interest: The authors declare no conflict of interest.

References

1. Burschka, J.; Pellet, N.; Moon, S.-J.; Humphry-Baker, R.; Gao, P.; Nazeeruddin, M.K.; Grätzel, M. Sequential deposition as a route to high-performance perovskite-sensitized solar cells. *Nature* **2013**, *499*, 316–319. [CrossRef] [PubMed]
2. Gao, P.; Grätzel, M.; Nazeeruddin, M.K. Organohalide lead perovskites for photovoltaic applications. *Energy Environ. Sci.* **2014**, *7*, 2448–2463. [CrossRef]
3. Salah, M.M.; Abouelatta, M.; Shaker, A.; Hassan, K.M.; Saeed, A. A comprehensive simulation study of hybrid halide perovskite solar cell with copper oxide as HTM. *Semicond. Sci. Technol.* **2019**, *34*, 115009. [CrossRef]
4. Kojima, A.; Teshima, K.; Shirai, Y.; Miyasaka, T. Organometal Halide Perovskites as Visible-Light Sensitizers for Photovoltaic Cells. *J. Am. Chem. Soc.* **2009**, *131*, 6050–6051. [CrossRef]
5. NREL, 2022. Best Research-Cell Efficiency Chart. Available online: https://www.nrel.gov/pv/cell-efficiency.html. (accessed on 27 November 2022).
6. Zhao, P.; Su, J.; Lin, Z.; Wang, J.; Zhang, J.; Hao, Y.; Ouyang, X.; Chang, J. All-Inorganic $CsPbI_xBr_{3-x}$ Perovskite Solar Cells: Crystal Anisotropy Effect. *Adv. Theory Simul.* **2020**, *3*, 2000055. [CrossRef]

7. Chen, L.; Wan, L.; Li, X.; Zhang, W.; Fu, S.; Wang, Y.; Li, S.; Wang, H.-Q.; Song, W.; Fang, J. Inverted All-Inorganic $CsPbI_2Br$ Perovskite Solar Cells with Promoted Efficiency and Stability by Nickel Incorporation. *Chem. Mater.* **2019**, *31*, 9032–9039. [CrossRef]
8. Conings, B.; Drijkoningen, J.; Gauquelin, N.; Babayigit, A.; D'Haen, J.; D'Olieslaeger, L.; Ethirajan, A.; Verbeeck, J.; Manca, J.; Mosconi, E.; et al. Intrinsic Thermal Instability of Methylammonium Lead Trihalide Perovskite. *Adv. Energy Mater.* **2015**, *5*, 1500477. [CrossRef]
9. Qiu, Z.; Li, N.; Huang, Z.; Chen, Q.; Zhou, H. Recent Advances in Improving Phase Stability of Perovskite Solar Cells. *Small Methods* **2020**, *4*, 1900877. [CrossRef]
10. Han, Q.; Bae, S.; Sun, P.; Hsieh, Y.; Yang, Y.; Rim, Y.S.; Zhao, H.; Chen, Q.; Shi, W.; Li, G. Single Crystal Formamidinium Lead Iodide ($FAPbI_3$): Insight into the Structural, Optical, and Electrical Properties. *Adv. Mater.* **2016**, *28*, 2253–2258. [CrossRef]
11. Liu, C.; Zhang, L.; Li, Y.; Zhou, X.; She, S.; Wang, X.; Tian, Y.; Jen, A.K.Y.; Xu, B. Highly Stable and Efficient Perovskite Solar Cells with 22.0% Efficiency Based on Inorganic–Organic Dopant-Free Double Hole Transporting Layers. *Adv. Funct. Mater.* **2020**, *30*, 2000967. [CrossRef]
12. Liu, C.; Li, W.; Zhang, C.; Ma, Y.; Fan, J.; Mai, Y. All-Inorganic $CsPbI_2Br$ Perovskite Solar Cells with High Efficiency Exceeding 13%. *J. Am. Chem. Soc.* **2018**, *140*, 3825–3828. [CrossRef] [PubMed]
13. Sutton, R.J.; Eperon, G.E.; Miranda, L.; Parrott, E.S.; Kamino, B.A.; Patel, J.B.; Hörantner, M.T.; Johnston, M.B.; Haghighirad, A.A.; Moore, D.T.; et al. Bandgap-Tunable Cesium Lead Halide Perovskites with High Thermal Stability for Efficient Solar Cells. *Adv. Energy Mater.* **2016**, *6*, 1502458. [CrossRef]
14. Wang, J.; Zhang, J.; Zhou, Y.; Liu, H.; Xue, Q.; Li, X.; Chueh, C.C.; Yip, H.L.; Zhu, Z.; Jen, A.K. Highly efficient all-inorganic perovskite solar cells with suppressed non-radiative recombination by a Lewis base. *Nat. Commun.* **2020**, *11*, 177. [CrossRef] [PubMed]
15. Jiang, Y.; Yuan, J.; Ni, Y.; Yang, J.; Wang, Y.; Jiu, T.; Yuan, M.; Chen, J. Reduced-Dimensional α-$CsPbX_3$ Perovskites for Efficient and Stable Photovoltaics. *Joule* **2018**, *2*, 1–13. [CrossRef]
16. Li, B.; Zhang, Y.; Fu, L.; Yu, T.; Zhou, S.; Zhang, L.; Yin, L. Surface passivation engineering strategy to fully-inorganic cubic $CsPbI_3$ perovskites for high-performance solar cells. *Nat. Commun.* **2018**, *9*, 1076. [CrossRef]
17. Tian, J.; Xue, Q.; Tang, X.; Chen, Y.; Li, N.; Hu, Z.; Shi, T.; Wang, X.; Huang, F.; Brabec, C.J.; et al. Dual Interfacial Design for Efficient $CsPbI_2$ Br Perovskite Solar Cells with Improved Photostability. *Adv. Mater.* **2019**, *31*, 1901152. [CrossRef]
18. Tao, S.; Schmidt, I.; Brocks, G.; Jiang, J.; Tranca, I.; Meerholz, K.; Olthof, S. Absolute energy level positions in tin- and lead-based halide perovskites. *Nat. Commun.* **2019**, *10*, 2560. [CrossRef]
19. Lau, C.F.J.; Wang, Z.; Sakai, N.; Zheng, J.; Liao, C.H.; Green, M.; Huang, S.; Snaith, H.J.; Ho-Baillie, A. Fabrication of Efficient and Stable $CsPbI_3$ Perovskite Solar Cells through Cation Exchange Process. *Adv. Energy Mater.* **2019**, *9*, 1901685. [CrossRef]
20. Gan, Y.; Zhao, D.; Qin, B.; Bi, X.; Liu, Y.; Ning, W.; Yang, R.; Jiang, Q. Numerical Simulation of High-Performance $CsPbI_3$/$FAPbI_3$ Heterojunction Perovskite Solar Cells. *Energies* **2022**, *15*, 7301. [CrossRef]
21. Chen, W.; Zhang, J.; Xu, G.; Xue, R.; Li, Y.; Zhou, Y.; Hou, J.; Li, Y. A Semitransparent Inorganic Perovskite Film for Overcoming Ultraviolet Light Instability of Organic Solar Cells and Achieving 14.03% Efficiency. *Adv. Mater.* **2018**, *30*, e1800855. [CrossRef]
22. Liu, S.; Chen, W.; Shen, Y.; Wang, S.; Zhang, M.; Li, Y.; Li, Y. An intermeshing electron transporting layer for efficient and stable $CsPbI_2Br$ perovskite solar cells with open circuit voltage over 1.3 V. *J. Mater. Chem. A* **2020**, *8*, 14555–14565. [CrossRef]
23. Ho-Baillie, A.; Zhang, M.; Lau, C.F.J.; Ma, F.-J.; Huang, S. Untapped Potentials of Inorganic Metal Halide Perovskite Solar Cells. *Joule* **2019**, *3*, 938–955. [CrossRef]
24. Eperon, G.E.; Paterno, G.M.; Sutton, R.J.; Zampetti, A.; Haghighirad, A.A.; Cacialli, F.; Snaith, H.J. Inorganic caesium lead iodide perovskite solar cells. *J. Mater. Chem. A* **2015**, *3*, 19688–19695. [CrossRef]
25. Che, Y.; Liu, Z.; Duan, Y.; Wang, J.; Yang, S.; Xu, D.; Xiang, W.; Wang, T.; Yuan, N.; Ding, J.; et al. Hydrazide Derivatives for Defect Passivation in Pure $CsPbI_3$ Perovskite Solar Cells. *Angew. Chem. Int. Ed.* **2022**, *61*, 202205012. [CrossRef] [PubMed]
26. Tan, S.; Yu, B.; Cui, Y.; Meng, F.; Huang, C.; Li, Y.; Chen, Z.; Wu, H.; Shi, J.; Luo, Y.; et al. Temperature-Reliable Low-Dimensional Perovskites Passivated Black-Phase $CsPbI_3$ toward Stable and Efficient Photovoltaics. *Angew. Chem.* **2022**, *61*, 202201300. [CrossRef]
27. Liu, X.; Lian, H.; Zhou, Z.; Zou, C.; Xie, J.; Zhang, F.; Yuan, H.; Yang, S.; Hou, Y.; Yang, H.G. Stoichiometric Dissolution of Defective $CsPbI_2$ Br Surfaces for Inorganic Solar Cells with 17.5% Efficiency. *Adv. Energy Mater.* **2022**, *12*, 2103933. [CrossRef]
28. Duan, C.; Wen, Q.; Fan, Y.; Li, J.; Liu, Z.; Yan, K. Improving the stability and scalability of all-inorganic inverted CsPbI2Br perovskite solar cell. *J. Energy Chem.* **2022**, *68*, 176–183. [CrossRef]
29. Wang, K.; Su, Z.; Chen, Y.; Qi, H.; Wang, T.; Wang, H.; Zhang, Y.; Cao, L.; Ye, Q.; Huang, F.; et al. Dual bulk and interface engineering with ionic liquid for enhanced performance of ambient-processed inverted CsPbI3 perovskite solar cells. *J. Mater. Sci. Technol.* **2022**, *114*, 165–171. [CrossRef]
30. Li, T.; Wu, Y.; Liu, Z.; Yang, Y.; Luo, H.; Li, L.; Chen, P.; Gao, X.; Tan, H. Cesium acetate-assisted crystallization for high-performance inverted CsPbI3 perovskite solar cells. *Nanotechnology* **2022**, *33*, 375205. [CrossRef]
31. Li, X.; Zhang, W.; Guo, X.; Lu, C.; Wei, J.; Fang, J. Constructing heterojunctions by surface sulfidation for efficient inverted perovskite solar cells. *Science* **2022**, *375*, 434–437. [CrossRef]
32. Chen, L.; Yin, Z.; Mei, S.; Xiao, X.; Wang, H.-Q. Enhanced photoelectric performance of inverted CsPbI2Br perovskite solar cells with zwitterion modified ZnO cathode interlayer. *J. Power Sources* **2021**, *499*, 229909. [CrossRef]

33. Fu, S.; Sun, N.; Le, J.; Zhang, W.; Miao, R.; Zhang, W.; Kuang, Y.; Song, W.; Fang, J. Tailoring Defects Regulation in Air-Fabricated $CsPbI_3$ for Efficient Inverted All-Inorganic Perovskite Solar Cells with V_{oc} of 1.225 V. *ACS Appl. Mater. Interfaces* **2022**, *14*, 30937–30945. [CrossRef] [PubMed]
34. Martin, R.M. *Electronic Structure: Basic Theory and Practical Methods*; Cambridge University Press: Cambridge, UK, 2004.
35. Madsen, G.K.H.; Blaha, P.; Schwarz, K.; Sjöstedt, E.; Nordström, L. Efficient linearization of the augmented plane-wave method. *Phys. Rev. B* **2001**, *64*, 195134. [CrossRef]
36. Blaha, P.; Schwarz, K.; Madsen, G.; Kvasnicka, D.; Luitz, J. *WIEN2k: An Augmented Plan Wave Plus Local Orbitals Program for Calculating Crystal Properties*; Vienna University of Technology: Vienna, Austria, 2014.
37. Perdew, J.P.; Burke, K.; Ernzerhof, M. Generalized gradient approximation made simple. *Phys. Rev. Lett.* **1996**, *77*, 3865–3868. [CrossRef] [PubMed]
38. Heyd, J.; Scuseria, G.E.; Ernzerhof, M. Hybrid functionals based on a screened Coulomb potential. *J. Chem. Phys.* **2003**, *118*, 8207–8215, Erratum in *J. Chem. Phys.* **2006**, *124*, 219906. [CrossRef]
39. Wang, B.; Novendra, N.; Navrotsky, A. Energetics, Structures, and Phase Transitions of Cubic and Orthorhombic Cesium Lead Iodide ($CsPbI_3$) Polymorphs. *J. Am. Chem. Soc.* **2019**, *141*, 14501–14504. [CrossRef]
40. Trots, D.M.; Myagkota, S.V. High-temperature structural evolution of caesium rubidium triiodoplumbates. *J. Phys. Chem. Solids* **2008**, *69*, 2520–2526. [CrossRef]
41. Beal, R.E.; Slotcavage, D.J.; Leijtens, T.; Bowring, A.R.; Belisle, R.A.; Nguyen, W.H.; Burkhard, G.F.; Hoke, E.T.; McGehee, M.D. Cesium Lead Halide Perovskites with Improved Stability for Tandem Solar Cells. *J. Phys. Chem. Lett.* **2016**, *7*, 746–751. [CrossRef]
42. Swarnkar, A.; Marshall, A.R.; Sanehira, E.M.; Chernomordik, B.D.; Moore, D.T.; Christians, J.A.; Chakrabarti, T.; Luther, J.M. Quantum dot–induced phase stabilization of α-$CsPbI_3$ perovskite for high-efficiency photovoltaics. *Science* **2016**, *354*, 92–95. [CrossRef]
43. Paul, T.; Chatterjee, B.K.; Maiti, S.; Sarkar, S.; Besra, N.; Das, B.K.; Panigrahi, K.J.; Thakur, S.; Ghorai, U.K.; Chattopadhyay, K.K. Tunable cathodoluminescence over the entire visible window from all-inorganic perovskite $CsPbX_3$ 1D architecture. *J. Mater. Chem. C* **2018**, *6*, 3322–3333. [CrossRef]
44. He, M.; Ding, L.; Liu, S.; Shao, G.; Zhang, Z.; Liang, X.; Xiang, W. Superior fluorescence and high stability of B-Si-Zn glasses based on Mn-doped CsPbBrxI3-x nanocrystals. *J. Alloys Compd.* **2019**, *780*, 318–325. [CrossRef]
45. Zhuang, J.; Wei, Y.; Luan, Y.; Chen, N.; Mao, P.; Cao, S.; Wang, J. Band engineering at the interface of all-inorganic $CsPbI_2Br$ solar cells. *Nanoscale* **2019**, *11*, 14553–14560. [CrossRef] [PubMed]
46. Ghosh, D.; Ali, Y.; Chaudhary, D.K.; Bhattacharyya, S. Dependence of halide composition on the stability of highly efficient all-inorganic cesium lead halide perovskite quantum dot solar cells. *Sol. Energy Mater. Sol. Cells* **2018**, *185*, 28–35. [CrossRef]
47. Burgelman, M.; Nollet, P.; Degrave, S. Modelling polycrystalline semiconductor solar cells. *Thin Solid Films* **2000**, *361–362*, 527–532. [CrossRef]
48. Adhikari, K.R.; Gurung, S.; Bhattarai, B.K.; Soucase, B.M. Comparative study on $MAPbI_3$ based solar cells using different electron transporting materials. *Phys. Status Solidi* **2016**, *13*, 13–17. [CrossRef]
49. Chakraborty, K.; Choudhury, M.G.; Paul, S. Numerical study of Cs2TiX6 (X = Br−, I−, F− and Cl−) based perovskite solar cell using SCAPS-1D device simulation. *Sol. Energy* **2019**, *194*, 886–892. [CrossRef]
50. Tahiri, O.; Kassou, S.; Ettakni, M.; Belaaraj, A. Simulation studies of lead-free Mn-based 2D perovskite solar cells. *Semicond. Sci. Technol.* **2021**, *36*, 095043. [CrossRef]
51. Lin, L.; Jiang, L.; Li, P.; Xiong, H.; Kang, Z.; Fan, B.; Qiu, Y. Simulated development and optimized performance of CsPbI3 based all-inorganic perovskite solar cells. *Sol. Energy* **2020**, *198*, 454–460. [CrossRef]
52. Casas, G.; Cappelletti, M.; Cédola, A.; Soucase, B.M.; Blancá, E.P.Y. Analysis of the power conversion efficiency of perovskite solar cells with different materials as Hole-Transport Layer by numerical simulations. *Superlattices Microstruct.* **2017**, *107*, 136–143. [CrossRef]
53. Son, H.; Jeong, B.-S. Optimization of the Power Conversion Efficiency of $CsPbI_xBr_{3-x}$-Based Perovskite Photovoltaic Solar Cells Using ZnO and NiO_x as an Inorganic Charge Transport Layer. *Appl. Sci.* **2022**, *12*, 8987. [CrossRef]
54. Azri, F.; Meftah, A.; Sengouga, N.; Meftah, A. Electron and hole transport layers optimization by numerical simulation of a perovskite solar cell. *Sol. Energy* **2019**, *181*, 372–378. [CrossRef]
55. Deng, Q.; Li, Y.; Chen, L.; Wang, S.; Wang, G.; Sheng, Y.; Shao, G. The effects of electron and hole transport layer with the electrode work function on perovskite solar cells. *Mod. Phys. Lett. B* **2016**, *30*. [CrossRef]
56. Hossain, M.I.; Alharbi, F.H.; Tabet, N. Copper oxide as inorganic hole transport material for lead halide perovskite based solar cells. *Sol. Energy* **2015**, *120*, 370–380. [CrossRef]
57. Nama Manjunatha, K.; Paul, S. Investigation of optical properties of nickel oxide thin films deposited on different substrates. *Appl. Surf. Sci.* **2015**, *352*, 10–15. [CrossRef]
58. Behrouznejad, F.; Shahbazi, S.; Taghavinia, N.; Wu, H.-P.; Diau, E.W.-G. A study on utilizing different metals as the back contact of $CH_3NH_3PbI_3$ perovskite solar cells. *J. Mater. Chem. A* **2016**, *4*, 13488–13498. [CrossRef]
59. Shao, S.; Loi, M.A. The Role of the Interfaces in Perovskite Solar Cells. *Adv. Mater. Interfaces* **2020**, *7*, 1901469. [CrossRef]